Mixing processes in the transonic, accelerated wake of a central injector

J. Richter,[1, a)] M. Beuting,[2] C. Schulz,[2] and B. Weigand[1]
[1)] *Institute of Aerospace Thermodynamics, University of Stuttgart, Stuttgart, Germany*
[2)] *Institute for Combustion and Gas Dynamics – Reactive Fluids, University of Duisburg-Essen, Duisburg, Germany*

(Dated: 11 September 2018)

The compressible accelerated mixing layer of a central injector was investigated experimentally and numerically. A wing-shaped central injector was mounted upstream of a rectangular convergent-divergent nozzle, through which air was accelerated to a Mach number of 1.7. The free-stream Reynolds number at the point of injection was 6.245×10^4. Four different measurement techniques – short-time illuminated schlieren imaging, laser schlieren, laser-induced thermal acoustics (LITA), and laser-induced fluorescence (LIF) – were applied to visualize the flow structures and to measure the predominant frequency of periodic flow features, the Mach number and temperature, and the injectant distribution. In addition, three-dimensional (3D) unsteady Reynolds-averaged Navier-Stokes (URANS) simulations using the shear stress transport (SST) turbulence model were conducted. Instantaneous images showed that the mixing layer was dominated by a series of alternating vortices. We were able to prove the mixing layer's self-similarity by means of injectant mass fraction profiles, which were derived from LIF measurements. The growth rate of the mixing layer was shown to approximately follow the $^1/_2$-power law. It was concluded from comparison to literature data that the growth rate is primarily determined by the free-stream Reynolds number, whereas the free-stream Mach number (compressibility effects) and the injectant amount play a minor role. Numerical simulations showed overall good agreement with the experimental data. However, the vortex shedding frequency and the mixing layer growth rate were underestimated by the simulations, as well as the wake deficit derived from Mach number profiles, which were measured with LITA. This indicates that the flow physics of vortex formation are not entirely reproduced.

Keywords: Transonic mixing layer, blunt-body wake, schlieren imaging (SI), laser schlieren (LS), laser-induced thermal acoustics (LITA), laser-induced fluorescence (LIF) imaging, 3D URANS simulation

I. INTRODUCTION

Efficient and rapid mixing of two or more reactants is of central importance for numerous technical applications. Their special demands involve a variety of technical implementations, one of these being a central injector through which a gas is injected parallel into a gaseous coflow. Such wake flows have drawn scientific interest over the last decades. However, most research has been conducted in either purely sub-[1–7] or supersonic flows[8–10] due to their technical relevance, e.g., heat transfer enhancement and scramjets.

In incompressible planar wakes, large-scale streamwise vortices that periodically shed from the upper and lower shear layer are the principle mechanism of entrainment and mixing. It was shown that the vortex shedding frequency scales linearly with the free-stream velocity over a wide Reynolds number range[1,2,11], and that the normalized shape of the deficit velocity profile remains invariant regardless of the shape of the wake generator.[3,12] The effect of a splitter plate that separates the shear layers[4,5] as well as the impact of base bleed[6,7] have been extensively studied. Both were shown to delay or even suppress the onset of vortex shedding, depending on the length of the splitter plate/the amount of injectant added to the wake.

[a)] Electronic mail: judith.richter@itlr.uni-stuttgart.de

The effect of compressibility has been addressed by means of two-stream shear layers.[8,9] It could be demonstrated that compressibility inhibits turbulent diffusion and, as a consequence, significantly reduces the growth rate. Nevertheless, the self-preserving state of the wake structures persist also in supersonic wake flows.[10]

More recently, transonic mixing investigations[13–15] emerged from a research activity devoted to the development of a shock-wave flow reactor to synthesize nanoparticles.[16] It features a central injector through which a precursor is injected into the subsonic flow region of a convergent-divergent nozzle. The principle idea is to initiate the particle formation by a controlled shock wave downstream of the nozzle throat to achieve a narrow size distribution. This requires a spatially and temporally homogeneous mixture, thus efficient and rapid mixing within the convergent-divergent nozzle. Previous studies in our lab suggest that the mixing layer stays invariant despite of the strong flow gradients within the nozzle and independent of the injection angle and shape of the central injector (with/without streamwise ramps).[13,14] Large eddy simulations[15] revealed that an injector configuration with a streamwise-ramp geometry outperforms its planar counterpart regarding the mixing quality. However, the wake growth rate was noticeably reduced[13] because the introduction of spanwise vorticity weakens the large-scale coherent structures.

All these studies on transonic mixing processes shared the same goals defined by gas-dynamically induced nanoparticle synthesis. As a consequence, the geometry of the flow channel was predetermined and did not allow for fundamental investigations of the underlaying flow physics. Very recently, a new modular flow channel has been designed at University of Stuttgart to experimentally study the mixing behavior of a compressible accelerated nozzle flow under controlled flow conditions.[17–22] The main objective of our current investigation is to provide a profound experimental data set involving different measurement techniques that can be used as validation of numerical simulations.

This paper reports on combined experimental and numerical mixing investigations in the wake of a central injector that is located upstream of a convergent-divergent nozzle. Four different measurement techniques – short-time illuminated schlieren imaging (SI), laser schlieren (LS), laser-induced thermal acoustics (LITA), and laser-induced fluorescence (LIF) imaging – were applied to visualize the flow structures and to measure the vortex shedding frequency, the Mach number and temperature, and the injectant distribution. These experimental results are used for the validation of three-dimensional (3D) unsteady Reynolds-averaged Navier-Stokes (URANS) simulations. It could be shown that the simulations globally yield satisfactory results, but fail to correctly predict the onset of vortex shedding.

The following section will provide details on the experimental and numerical setup and on the measurement techniques applied. The results section will first show instantaneous images of the flow structures together with results from vortex shedding frequency measurements. This will be followed by a detailed discussion of results from LITA (Mach number and temperature) and LIF (injectant distribution) measurements including evidence of the self-preserving state of the mixing layer. Further, numerical results will be provided throughout the results section. The discussion section will involve comparison of the LIF results to previous measurements and will give possible reasons for the deviation between numerical and experimental results. Finally, all major findings will be summarized and concluded.

II. METHODS

A. Experimental Methods

All experiments were performed at the high-enthalpy flow facility (Fig. 1) of the Institute of Aerospace Thermodynamics (ITLR) at the University of Stuttgart. It includes a screw compressor and an air dryer that can continuously deliver up to 1.45 $\mathrm{kg\,s^{-1}}$ dry air at a maximum total pressure of 10 bar. The air can be heated electrically to a maximum total temperature of 1300 K before entering the flow channel. Four decomissioned submarine air flasks function as an auxiliary air supply in case of breakdown of the screw compressor. The test facility is further equipped with a mass flow meter (Endress + Hauser, Prowirl 77H DN 100, accuracy < 1% of reading) and a pressure sensor (Omega, PAA21-C-10, accuracy < 0.5% of full scale), which measures the total pressure at the flange connection between the heater outlet and the flow channel inlet.

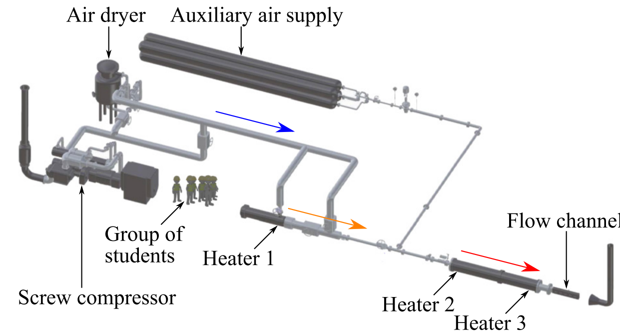

FIG. 1. High-enthalpy flow facility at the University of Stuttgart

1. Modular flow channel

The modular flow channel has a constant width of 40 mm and consists of three segments and an outlet diffuser. Its modular design allows to vary the injector geometry and position, the pressure gradient downstream of the nozzle, and the nozzle Mach number. This paper focuses on one specific configuration as described below.

Figure 2 shows the cross-section through the middle plane of the modular flow channel. The first module connects the heater exit with the optically accessible test section (modules 2 and 3). It provides eight ports for main flow seeding, four of which were utilized to evenly inject tracer into the main flow for *insitu* flat-field correction of the LIF images: Two pipes of 5 mm in diameter that feature ten bores (d = 0.7 mm) were each horizontally plugged through the flow channel and seeded with tracer from both channel sides. The first module is further equipped with a temperature probe union that is employed to position a calibrated thermocouple (type K, accuracy ±1.5 K) at the flow centerline to measure the total temperature of the main flow.

The second module includes the central injector and the convergent-divergent nozzle, through which the main flow is accelerated to a Mach number of about 1.7. Figure 3 shows the geometry and dimensions of the central injector. It is wing-shaped, extends over the entire width of the channel and reaches down to 42.1 mm upstream of the nozzle throat. The injectant is added to the subsonic main flow through four holes of 2.5 mm in diameter spaced by a center-to-center distance of 4.8 mm. The second module further provides an extra port for additional measurement instrumentation, which was not used during the experiments presented here.

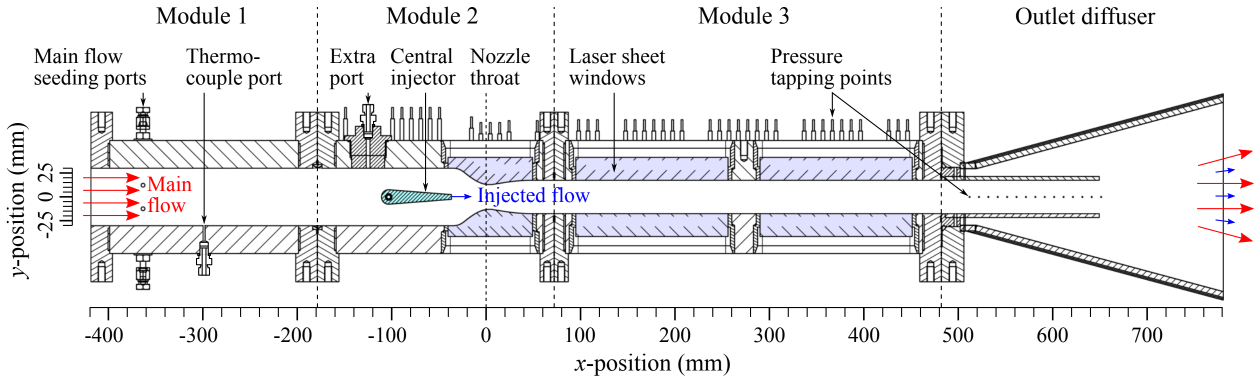

FIG. 2. Cross-section of the modular, rectangular (40 mm width) flow channel designed for transonic mixing investigations

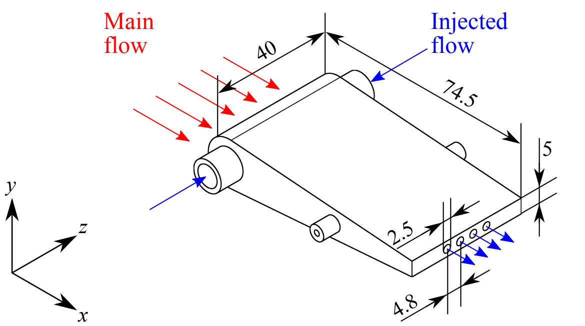

FIG. 3. Dimensions of the central injector

TABLE I. Injected gas flow conditions.

#	$\dot{m}_{\mathrm{INJ}}$ g/s	ξ_{air} –	ξ_{C7H8} –	ξ_{N2} –	$\dot{Q}_{\mathrm{INJ}}$ l/min	v_{INJ} m/s	Methods
1	0	0	0	0	0	0	LS
2	0.25	1	0	0	7.65	6.49	LS
3	0.50	1	0	0	15.30	12.99	LS, LITA, CFD
4	0.75	1	0	0	22.95	19.48	LS
5	1.00	1	0	0	30.60	25.98	LS
6	0.56	0	0.25	0.75	14.64	12.42	LS, LIF
7	0.75	0	0.40	0.60	17.13	14.54	LS, LIF, SI, CFD

The third module is basically a planar extension of the second module and allows for the observation of the mixing layer development. The last module functions as an outlet diffuser, which decelerates the flow to subsonic speed. To avoid deflection of the flow, two horizontal plates are mounted in its connecting flange (Fig. 2). Throughout modules 2 and 3, pressure taps (Scanivalve, DSA 3016, accuracy $< 0.05\%$ of full scale) are installed at the top wall slightly off the middle plane. Optical access is provided from all four sides to allow for the application of laser-induced fluorescence (LIF) imaging measurements.

The injected gas flow is provided by a heated evaporator system (Brooks DLI). The evaporator system is equipped with two mass flow controllers, one for the carrier gas (Brooks, GF40, accuracy $< 1\%$ of reading) and one for the liquid tracer (Brooks, QMBC, accuracy $< 0.5\%$ of reading), and with a calibrated thermocouple (type K, accuracy ± 1.5 K) just prior to the point of injection.

2. Flow conditions

During all experiments, air was provided at a total pressure of 2.5 bar and a total temperature of 380 K at the outlet of heater 3 (Fig. 1). The corresponding free-stream mass flow rate and the wall static pressure at the test section inlet ($x = -185$ mm) were $0.518\,\mathrm{kg\,s^{-1}}$ and 2.25 bar. The free-stream Reynolds number $\mathrm{Re}_\infty = u_\infty h_{\mathrm{ITE}}/\nu_\infty$ based on the height of the injector trailing edge h_{ITE} was calculated from numerical results to be 6.245×10^4. Here, u_∞ and ν_∞ are the free-stream velocity and kinematic viscosity at the boundary layer edge of the injector trailing edge.[21]

The injected gas flow was heated up to 380 K and consisted of, depending on the requirements of the measurement technique applied, pure air or a mixture of toluene (C_7H_8) and nitrogen (N_2), with mass fractions ξ_i of either 25 or 40 % toluene. The injected mass flow rate $\dot{m}_{\mathrm{INJ}}$ was varied to study the influence of the injector base bleed. All investigated injectant flow conditions are summarized in table I including the corresponding volume flow rate $\dot{Q}_{\mathrm{INJ}}$ and injection velocity v_{INJ}, which are calculated from the experimental conditions.

3. Optical measurement techniques

To evaluate different aspects of the mixing layer that develops downstream of the central injector, four different optical measurement techniques were applied: Short-time illuminated schlieren imaging (SI) was utilized to visualize the flow structures. A laser schlieren technique

(LS) was applied to determine the vortex shedding frequency. Laser-induced thermal acoustics (LITA) was used to quantitatively measure Mach number and temperature profiles close to the injector trailing edge. The mixing layer growth was analyzed qualitatively by applying laser-induced fluorescence (LIF) imaging using the added toluene as fluorescence target species. In the following, each measurement technique is briefly described.

A common schlieren setup[23], consisting of a green LED as a point light source, two achromatic lenses ($d = 100\,\mathrm{mm}$), a pinhole and an single-lens reflex (SLR) camera, was used to capture the high-frequency flow structures in the wake of the central injector. For this purpose, the LED light source was driven by a simple driver circuit[24] to emit high-power short-time pulses as short as $1\,\mu$s. For the current case, a light pulse with a duration of $5\,\mu$s showed best results regarding the balance of light output and blurring.

To measure the vortex shedding frequency in the mixing layer, a simple optical laser schlieren method that senses the density fluctuations induced by the vortices was applied.[18] The main principle is similar to that of schlieren imaging, the only difference being that the area of interest is significantly decreased. Therefore, the optical setup reduces to the following: A laser beam is aligned perpendicular to the flow direction at a point in the vicinity of the injector trailing edge. On the other side of the flow channel an iris and a high-speed photodetector, which is connected to an oscilloscope, are positioned in line with the laser beam. If necessary, a lens can be added between the laser source and the flow channel or/and just prior to the photodetector to locally reduce the beam diameter. The setup used for the experiments presented here is identical to that used in our previous experiments[18] except for the laser source, which was replaced by a low-cost fiber-coupled laser (Thorlabs, S1FC635, $\lambda = 635\,\mathrm{nm}$).

Laser-induced thermal acoustics (LITA, often also called laser-induced grating spectroscopy, LIGS) is a non-intrusive point measurement technique that can be applied to measure temperature, flow velocity, transport properties, species concentration, and pressure.[25,26] In brief, LITA is based on the scattering of a laser beam off a grating structure generated in the gaseous medium by interaction with two interfering pulsed laser beams:[27,28] Two coherent short-pulsed laser beams of the same power originating from a single laser source (pulsed Nd:YAG laser, Spectra-Physics PIV-200-10, $\lambda = 1064\,\mathrm{nm}$, $\tau_{pulse} = 10\,\mathrm{ns}$) intersect at a certain angle in the measurement volume to form an interference grating. This results in a spatially periodic modulation of the density of the test medium due to either the absorption and local heat-up of the test gas (resonant, thermalization) and/or the polarization of the molecules in the presence of an electrical field (non-resonant, electrostriction).[29] The initially formed grating dissipates with the local speed of sound and therefore causes a local temporal density fluctuation. A third laser beam from a second source (continuous wave DPSS laser, Coherent Verdi V8, $\lambda = 532\,\mathrm{nm}$) is focused on the interference grating and partly scattered, thus forming the signal beam. From its temporal variation, the speed of sound or, for a known composition of the test medium, the temperature can be derived from a frequency analysis. If the signal beam is mixed with its own unscattered part, the Doppler shift can be measured from the beat frequency, which contains information on the flow velocity. In the past, LITA has been applied at ITLR to measure Mach number and temperature in supersonic hydrogen/air diffusion flames, in shock-heated flows and in the supersonic wake of a strut injector.[30–32] In the experiments presented here, LITA was applied to measure Mach number and temperature profiles in the transonic, accelerated wake of a central injector, which requires the interference grating beeing oriented perpendicular to the flow. The measurement volume was always positioned within the x-y plane at the center of the flow channel (between the second and third injector hole, cf. Fig. 3), measured approximatly 0.3 mm in diameter, and extended 7 mm in z-direction. A detailed description of the optical setup and of the signal post-processing are given in one of our previous publications.[19]

Toluene laser-induced fluorescence (LIF) imaging was applied to measure the spatial distribution of the injected fluid in the wake of the central injector. The injectant consisted of vapor-phase toluene (C_7H_8) in nitrogen (N_2) and the toluene was excited by a $0.3\,\mathrm{mm} \times 24\,\mathrm{mm}$ laser light sheet at 248 nm from a krypton-fluoride excimer laser (Lambda Physics LPX100). The light sheet was positioned in the center of the channel illuminating the flow between the second and third injector hole (cf. Fig. 3). Its laser fluence was limited to $70\,\mathrm{mJ\,cm^{-2}}$ with a variable attenuator to ensure linear signal response. The toluene fluorescence that peaks at about 280 nm[33] was detected by an intensified CCD camera (LaVision Imager Intense + IRO) equipped with a bandpass filter ($280 \pm 20\,\mathrm{nm}$, Semrock BP280/20). More details are given in one of our previous publications.[20] For post-processing, the image data were mapped to real world coordinates, normalized with regard to the respective pulse laser energy, and time-averaged (200 shots). Further, averaged background and flat-field images were obtained to correct for scattered laser light and light sheet inhomogeneities. For the latter, toluene was fed far upstream into module 1 to achieve a homogeneous toluene concentration at experimental conditions. This was necessary because thermal expansion shifted the flow channel during startup and an approximate thermal equilibrium was only maintained if (hot) flow through the channel was present.

B. Numerical Methods

3D numerical simulations were performed to compare with the experimental data measured at inflow conditions #3 and #7 (table I). To minimize computational costs, the numerical domain was limited to $-185\,\mathrm{mm} \leq x \leq$

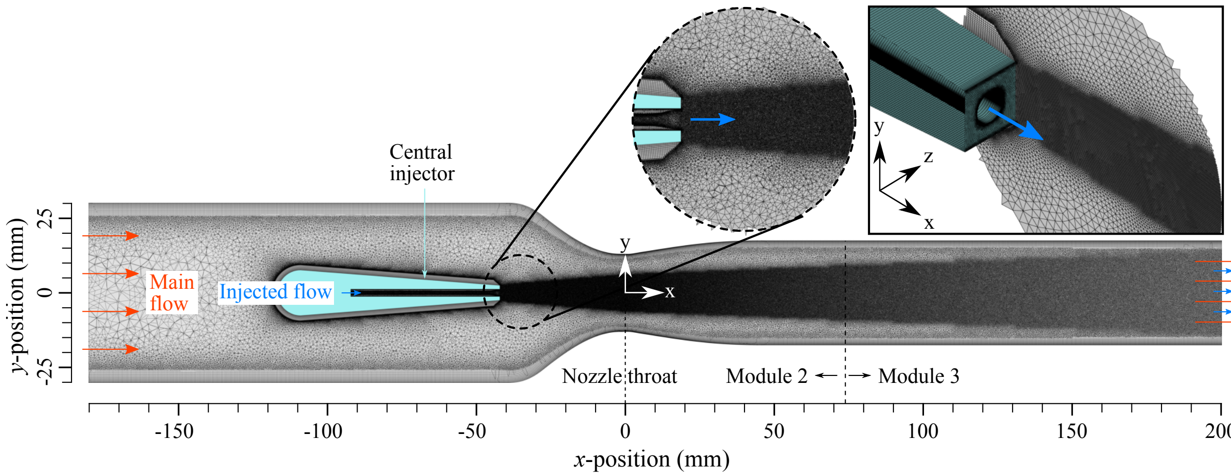

FIG. 4. Sketch of the 3D hybrid numerical mesh

200 mm corresponding to module 2 and about one third of module 3 (Fig. 2). In addition, only a single exit hole of the central injector was considered so that the spanwise extent of the domain was $\Delta z = 4.8\,\mathrm{mm}$ (Fig. 3). This was done by assuming periodicity in z-direction. A hybrid mesh of 8.65 Mio nodes that finely resolves the wake flow region was generated with CENTAUR 12.[34] Figure 4 shows a sketch of the entire grid and a detailed view of the cells in the vicinity of the injector trailing edge. The number of cells within the wall-near hex-layer varies locally between 15 and 28 to cover the changing boundary layer thickness. Further, the dimensionless wall distance $y_1^+ = y_w u_* / \nu$ stays within $30 < y_1^+ < 60$ everywhere, but in the injection bore where $y_1^+ < 2$. Here, y_w is the distance to the nearest wall, u_* is the friction velocity, and ν is the kinematic viscosity.

The unsteady Reynolds-averaged Navier-Stokes equations (URANS) were solved using the commercial implicit flow solver ANSYS CFX 18[35] and the shear stress transport (SST) turbulence model developed by Menter[36] was applied for describing the turbulent flow. The thermodynamic and transport properties of toluene (condition #7) were modeled in the form of least-squares coefficients according to NASA.[37] Further, the temperature dependence of its dynamic viscosity was evaluated with Refprop 10[38] and provided in the form of the Sutherland law. The physical time step was set to 1 µs in the case of condition #3 and to 0.5 µs in the case of condition #7 to ensure a maximum residuum below 10^{-4} for all relevant flow variables. The following boundary conditions were applied: Inflow profiles of total pressure p_0, total temperature T_0, turbulence intensity Tu, and eddy viscosity ratio ν_t/ν were calculated in a preceding simulation that covered module 1. Here, the experimental flow conditions (mass flow rate, total temperature, and wall static pressure at the test section inlet) were applied as boundary conditions, together with an initial turbulence intensity of 5% and an initial eddy viscosity ratio between the turbulent and molecular dynamic viscosity of 100. (We observed in one of our previous studies that a more elaborate choice of inlet turbulence level and viscosity ratio is not necessary since high turbulence is strongly damped within a short distance by the SST turbulence model.[19]) The mass flow injected through the central injector was set to either $0.125\,\mathrm{g\,s^{-1}}$ air (condition #3) or $0.1875\,\mathrm{g\,s^{-1}}$ toluene seeded nitrogen (condition #7) matching 1/4 of the injected mass flow in the experiments (through four injection holes). All flow channel and injector walls were treated as no slip, smooth walls and the outlet condition was set to supersonic flow.

Phase-averaged results are often required to compare with experimental data. Therefore, the numerical average was calculated over exactly five oscillations of vortex shedding after the simulation reached a quasi-steady state.

III. RESULTS

The results are organized in three parts: First, the dominant wake flow structures are identified from single-shot LIF images and short-time illuminated schlieren images. This part also contains results from frequency measurements within the wake obtained with the LS technique. Secondly, the most important flow properties (pressure, temperature, and velocity) are discussed including results from LITA measurements. Finally, the wake flow profiles and the axial growth rate of the wake are analyzed on the basis of time-averaged LIF data. All three parts further include results from 3D URANS simulations to compare with the particular experimental results.

The coordinate system used for processing and analysis of the data is located in the center of the nozzle throat as sketched in Fig. 4. Note that the distance to the injector trailing edge d may be used instead of the streamwise

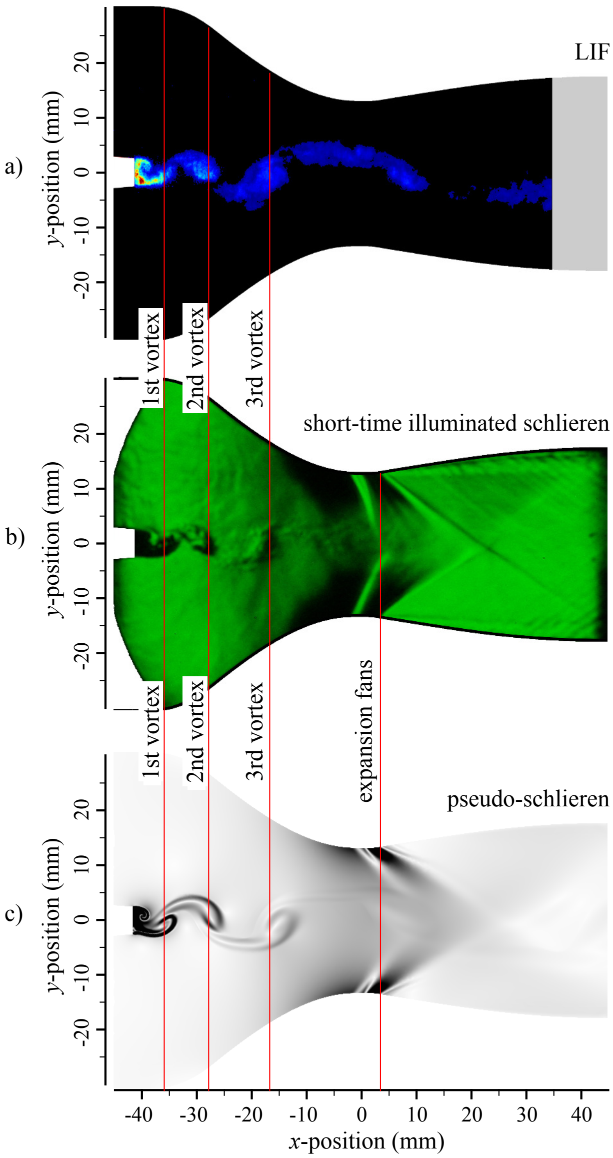

FIG. 5. Condition #7. a) single-shot LIF image, b) short-time illuminated schlieren image, and c) pseudo-schlieren image from numerical simulation of the wake and nozzle flow, all at the same phase angle. The injector trailing edge (white) is positioned at the very left side.

coordinate x ($d = x + 42.1\,\text{mm}$). Various mass flow rates and gas compositions were used as injection flow as summarized in table I. In the following, they will be referred with the numbers introduced in table I.

A. Wake flow structures

The shear layers of subsonic bluff body wakes are typically dominated by vortices that alternately shed from the upper and lower side of the wake generator. Such coherent structures have been observed downstream of the injector trailing edge in our experiments and numerical simulations. To experimentally visualize these high-frequency flow structures, short-time illuminated schlieren imaging was applied. Coherent structures could be also identified in single-shot LIF images since the vortices entrain most of the injected toluene. Figure 5 shows a single-shot LIF image, a schlieren image (experimental), and a pseudo-schlieren image (numerical) of the wake and nozzle flow at the same phase angle of vortex shedding.

The positions of the vortices downstream of the injector trailing edge agree very well. However, differences arise in the decay of the coherent structures. Apparently, the initially large vortices break up into smaller structures while being convected downstream. This can be concluded from the experimental images (Figs. 5a and b), where the vortices seem to disintegrate into smaller structures at their fringes. On the contrary, the (numerical) pseudo-schlieren image reveals very distinct vortices exhibiting a smooth shape. This is because turbulent structures are not resolved in the numerical (URANS) simulation.

The vortex shedding frequency f was measured with the LS setup (see above). The resulting Strouhal numbers $\text{St} = f h_{\text{ITE}}/u_\infty$ are plotted over the normalized base bleed rate $C_q = \dot{m}_{\text{INJ}}/(\rho_\infty u_\infty A_{\text{ITE}})$ in Fig. 6. Here, u_∞ and ρ_∞ are the free-stream velocity and density obtained from numerical simulation at the position of the injector trailing edge, and h_{ITE} and A_{ITE} are the height and the area of the injector trailing edge. The continuous lines in Fig. 6 approximate experimental results from Bearman[6] who investigated the effect of parallel injection through a slit-shaped opening on the wake of a blunt-trailing-edge model at similar Reynolds numbers. His model was designed with an exchangeable trailing edge to allow for the investigation of different slit heights, thus, of varying injection momentum (since the injection velocity increases with decreasing slit height). This variation is expressed in terms of the area ratio $A_{\text{INJ}}/A_{\text{ITE}}$, where A_{INJ} represents the injection opening and A_{ITE} the area of the trailing edge (including the injection opening). In our case, flow is injected through four holes instead of one slit (Fig. 3) and, consequently, the area ratio is smaller compared to that of Bearman.

The moderate (parallel) injection into the wake flow causes an increase of the vortex shedding frequency. This "stabilizing" effect is similar to that of a short splitter plate ($l/h_{\text{ITE}} \leq 1$) mounted at the trailing edge to separate the shear layers.[4] Beyond this, Bearman demonstrated that the velocity fluctuations become weak and irregular at higher mass flow rates ($C_q \geq 0.1$). However, the evaporator system that provided the base bleed in our experiments did not allow for larger C_q.

Figure 6 further shows results from numerical simulation (open symbols) for the two flow conditions #3 and #7. The predicted frequencies underestimate the vortex shedding frequencies by about 15 %. On a closer look at Fig. 5, one sees that the vortices visible in the pseudo-

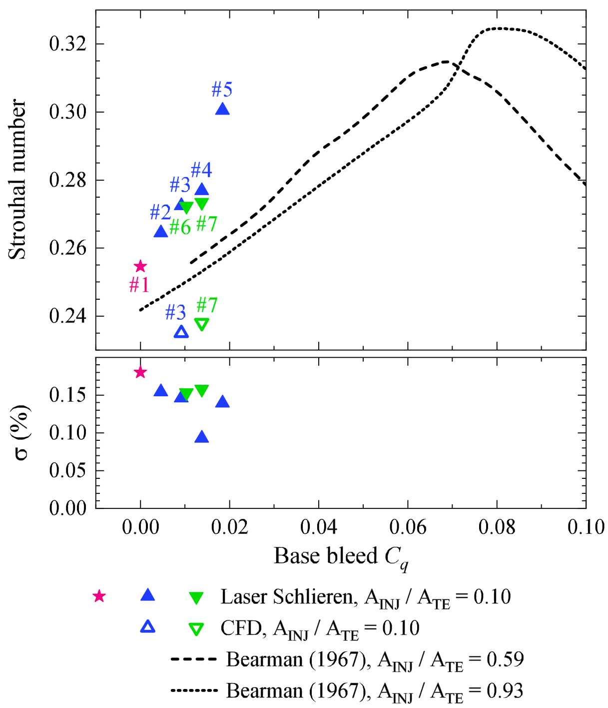

FIG. 6. Measured (laser schlieren, filled symbols) and simulated (CFD, open symbols) vortex shedding frequency without injection (condition #1, red), with air injection (conditions #2-5, blue), and with injection of toluene seeded nitrogen (conditions #6 and #7, green) at Re = 6.2×10^4 together with experimental results from Bearman[6] at Re = $2.3...4.1 \times 10^4$. The area ratio $A_{\mathrm{INJ}}/A_{\mathrm{ITE}}$ is a measure for the injection opening.

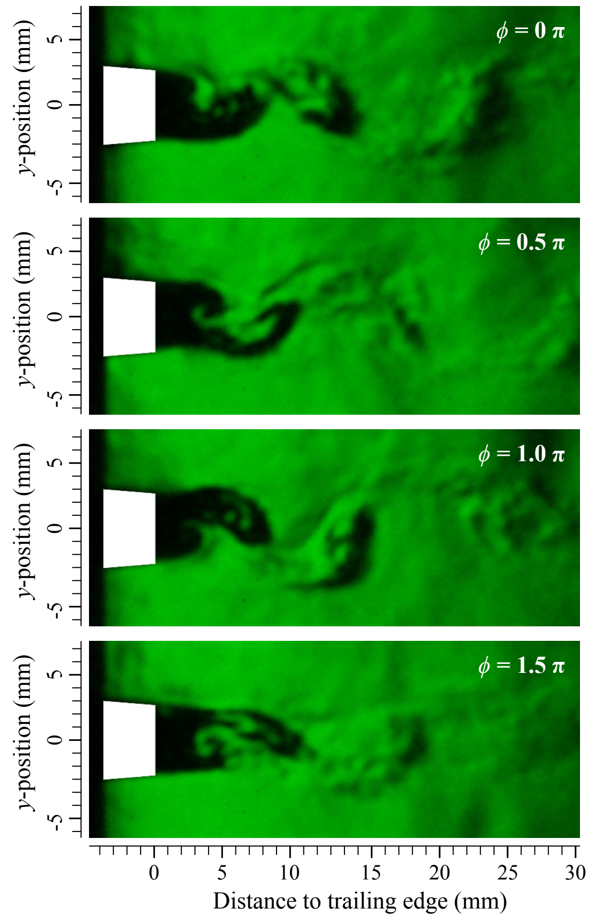

FIG. 7. Condition #7. Short-time illuminated schlieren images of the vortex formation at the injector trailing edge (white) representing four different phase angles ϕ over one oscillation cycle.

schlieren image (numerical) are slightly pulled apart – an effect of the lower frequency. This failure in frequency prediction was also observed for numerical simulations (2D URANS) without injection.[18]

Besides, injection into the wake flow causes a shift of the vortex formation point: In the case of no injection, the vortices form directly at the injector trailing edge, whereas with injection the vortices roll up further downstream from the edge of the shear layer.[7,18,21] The onset of vortex shedding is shown in detail in Fig. 7. The four images represent four different phase angles ϕ obtained from several oscillations. It nicely shows that the point of vortex formation is slightly detached from the injector trailing edge as a result of the low momentum injection.

B. Pressure, Mach number, and temperature

Figure 8 shows time-averaged wall static pressure measurements together with numerical results. Note that error bars are omitted as the confidence interval (less than ±0.035 bar) is smaller than the symbol size. The static pressure drops significantly from about 2.3 bar to about 0.5 bar while the main flow accelerates to supersonic speed. The numerical and experimental data agree nicely upstream of the third channel module ($x \leq 45$ mm). From there, downstream of the nozzle, the experiment reveals a rise in static wall pressure whereas the pressure stays approximately constant in the simulation. This deviation can be easily attributed to 3D effects, namely the side-wall boundary layers and the interaction between the boundary layers in the corners of the rectangular flow channel, which are not considered in the numerical domain. In addition, very weak oblique shock waves that form at the flange connection between module 2 and 3 ($x = 62.2$ mm) due to manufacturing inaccuracies were observed in the experiments.[22]

Temperature and Mach number profiles have been measured with LITA in the wake of the central injector along the nozzle center line (Fig. 9) and perpendicular to the flow direction (Fig. 10a-c). All data sets were recorded separately in consecutive measurement series within one day. Since the temperature is calculated from the speed of sound and, thus, depends on the gas composition (ideal gas law), the injectant added to the

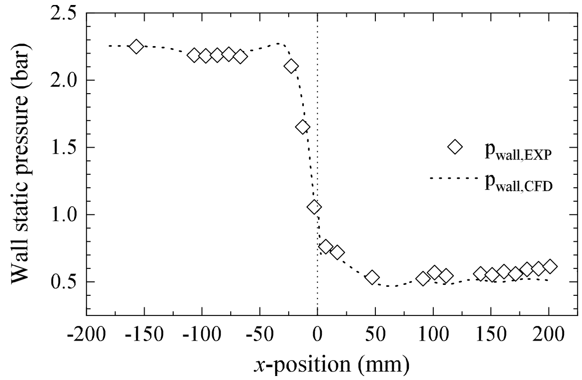

FIG. 8. Condition #7. Measured (EXP) and simulated (CFD) time-averaged wall static pressure.

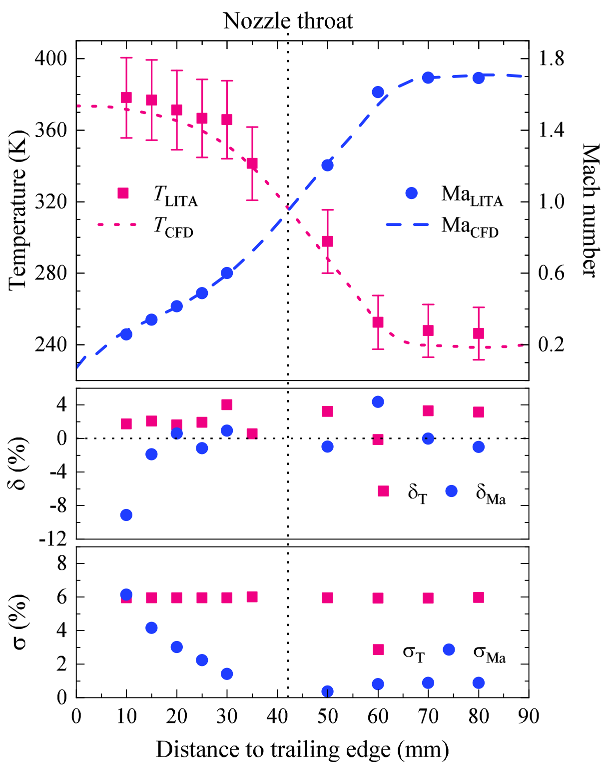

FIG. 9. Condition #3. Temperature and Mach number distribution along the nozzle centerline from LITA measurements together with results from numerical simulation (CFD), their discrepancy δ and the standard deviation of the experiments σ (66 % confidence interval).

wake was pure air (condition #3) to achieve a uniform gas composition throughout the flow channel. The error bars represent the standard deviation σ (66 % confidence interval) that was estimated according to previous investigations.[19] Note that the Mach number is a direct result of (heterodyne) LITA detection, whereas the temperature determination requires additional calibration and, as a consequence, its standard deviation is larger.

Figure 9 shows that similar to the wall static pressure (Fig. 8) the centerline temperature decreases from 378 ± 23 K to 246 ± 15 K as the flow is accelerated to supersonic speed. Further, the maximum Mach number measured at the nozzle exit amounts to 1.691 ± 0.015 and therefore meets the design Mach number of 1.7. The numerical results (dashed line) agree well with the measurements. The deviations δ are ≤ 4 % everywhere but close to the trailing edge at $d = 10$ mm, where the Mach number is underestimated by 8.3 %.

This discrepancy in centerline Mach number is also evident at the centerline position of the corresponding flow profile plotted in Fig. 10a, which originates from another, not the "centerline" but the "perpendicular" measurement series. Here, the deviation between experimental and numerical investigation is even larger and amounts to 25.7 %. Nevertheless, the error bars of both measurements from the two series almost overlap, cf. open and filled symbol in Fig. 10a. We believe that the deviation between these two series can have two reasons: First, the main flow conditions are subject to small fluctuations over the test day. Secondly, the flow channel shifts during the test day due to thermal expansion of the test facility adversely influencing the reproducability of the beam positioning. However, both measurements differ significantly from the simulated Mach number revealing that the numerical wake deficit is too small. This is not surprising since the deviation in shedding frequency (Fig. 6) already indicates that the wake flow physics are not entirely met. Apart from the centerline position, the recorded (LITA) Mach numbers at $d = 10$ mm are only slightly overestimated and the shape of the profiles agree reasonably well.

At $d = 30$ mm downstream of the injector trailing edge (Fig. 10b) the wake has broadened and, again, the simulated Mach numbers apparently underestimate the wake deficit. However, at 50 mm downstream of the injector trailing edge (Fig. 10c) both, the Mach number and the shape of the profile, match. Further downstream the signal quality degraded due to further decrease in pressure so that the evaluation became infeasible.[19] We believe that the reason why the only Mach number profile recorded in the supersonic flow region is better predicted by the numerical simulation is the following: Here, the minimum velocity at the centerline position does not primarily originate from the wake deficit itself, but from the supersonic nozzle flow profile. The velocity profile "flips" at the nozzle throat, i.e., its initial shape is reversed so that the minimum velocity occurs at the nozzle centerline. Compared to this, the wake deficit velocity is negligible.

Apart from the Mach number profiles, all predicted temperature profiles lie within the experimental confidence interval at all three positions (Figs. 10a-c). This is obviously favored by the large uncertainty and an improved measurement accuracy would be desired to better evaluate the numerical results. However, this requires *in-*

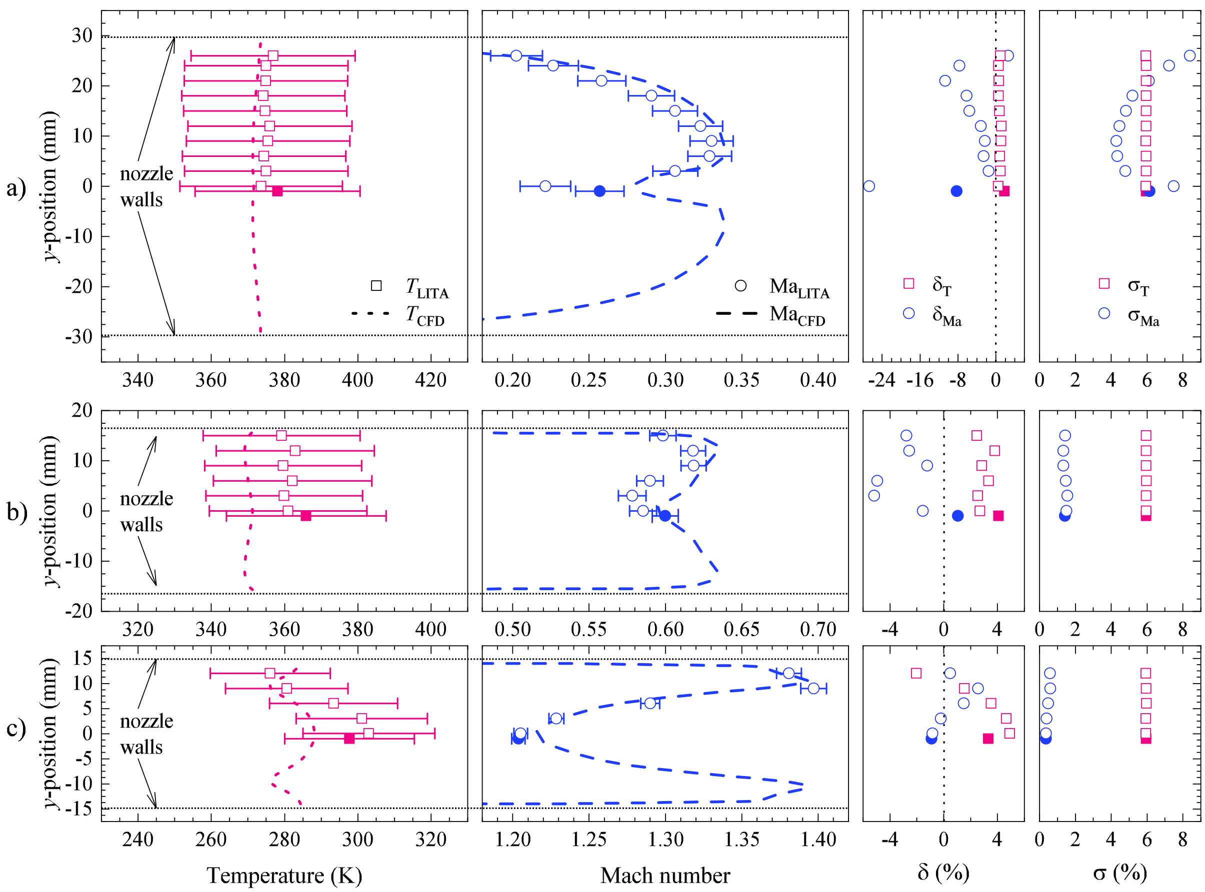

FIG. 10. Condition #3. Temperature and Mach number profiles at three different streamwise positions, a) 10 mm, b) 30 mm, and c) 50 mm downstream of the injector trailing edge, from LITA measurements together with results from numerical simulation (CFD), their discrepancy δ and the standard deviation of the experiments σ (66 % confidence interval). Filled symbols are results from the "centerline" measurement series (cf. Fig. 9), which are plotted for comparison.

situ calibration of the LITA setup[19], which is currently not possible at our facility.

C. Mixing layer growth

Wake flows are typically characterized by their deficit velocity and their half-width.[12] The latter is defined as the point perpendicular to the flow direction where the deficit velocity is reduced to 50%. With increasing distance to the wake generator, the deficit velocity decreases while the half-width increases. From these two properties, the axial growth rate of a wake can be determined. In most cases, the shape of the normalized deficit velocity profiles (normalized with respect to their maxima and the corresponding half-width) do not change from a certain point downstream of the wake generator regardless of its geometry.[1,3,13] This phenomenon is called self-similar behavior.

In order to experimentally visualize the mixing layer, toluene was added as a tracer to the injected gas flow (conditions #6 and #7) to allow for the application of tracer LIF. Figure 11 shows the resulting time-averaged LIF image composed of 11 light sheet positions that cover the first two windows of the flow channel (Fig. 2). (All images are normalized by the integrated signal-intensity in y-direction for illustration purposes.) It further sketches a LIF intensity profile extracted at an arbitrary position.

By analogy with the conventional wake flow analysis, the half-width $\delta_{1/2}$ equals the half-width half-maximum value of the intensity profile. Therefore, each profile is filtered and normalized by the maximum of the smoothed curve $I_{\max}$. As a result, the half-width can be derived from the point where the normalized intensity equals 0.5.

To compare with numerical results, the LIF intensity needs to be related to a flow property that is simulated, e.g., the normalized toluene mass fraction. The intensity of the LIF signal depends on, among others, the local flow temperature, static pressure and the oxygen partial pressure.[39–42] The latter strongly reduces the LIF signal due to collisional quenching by oxygen.[33] Therefore, the signal also depends on the mixing state on the molecular level of the injectant (oxygen-free) and the co-flow (air).

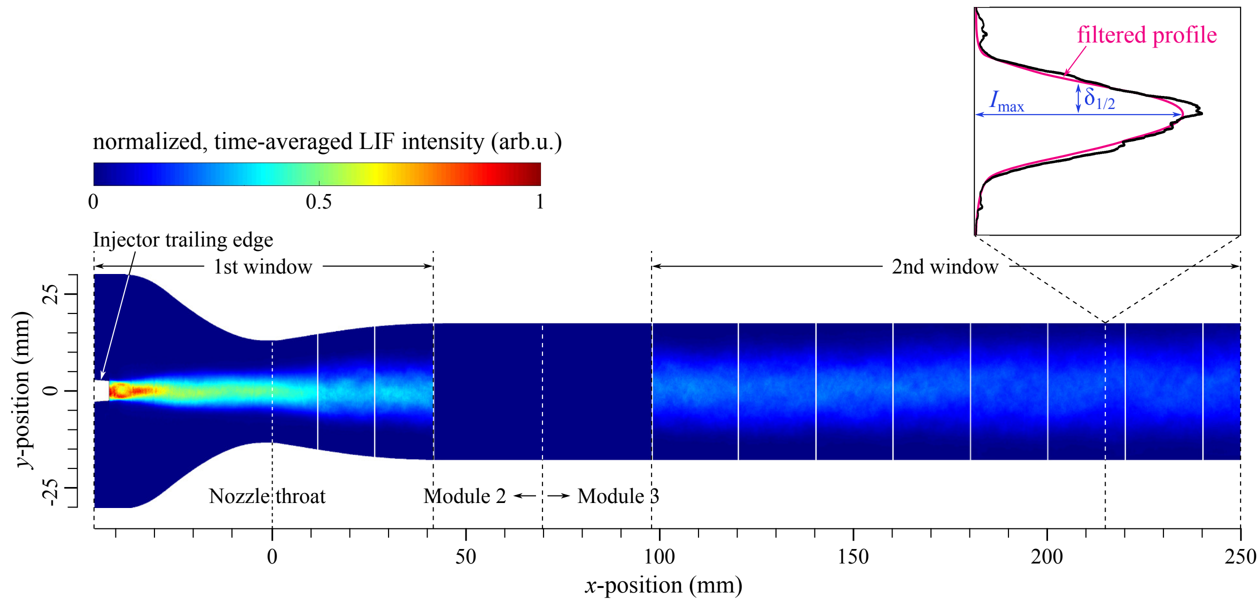

FIG. 11. Normalized (by the integrated intensity in y-direction at each x-position), time-averaged toluene-LIF image corrected for background signal and flat-field variations composed of 11 adjacent light sheet positions (as indicated by white thin lines). LIF intensity profiles are extracted at numerous streamwise positions and normalized with respect to their local maximum I_{max} and their local half-width $\delta_{1/2}$ as exemplary sketched at $x = 225$ mm.

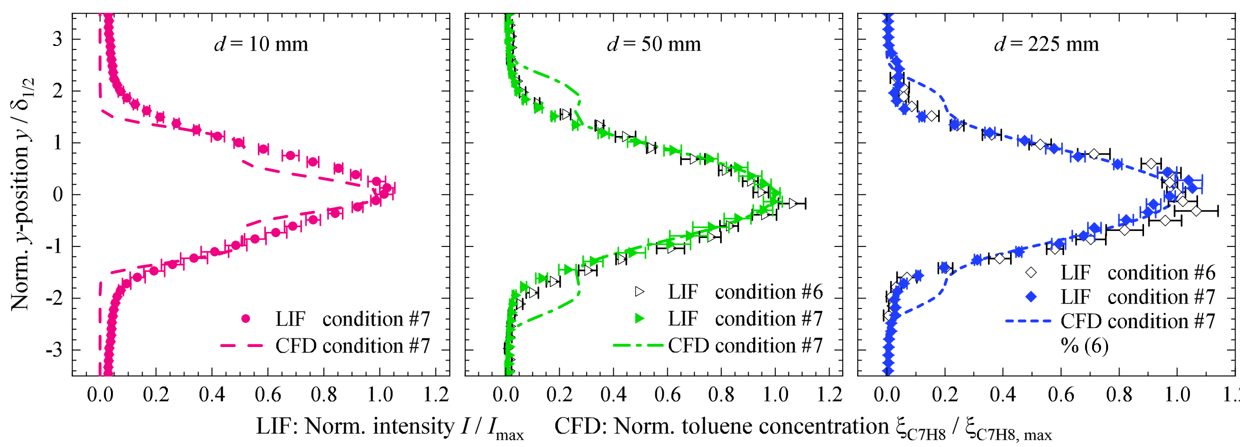

FIG. 12. Comparison of normalized LIF intensity profiles and normalized toluene (C_7H_8) mass fraction profiles from numerical simulations.

Assuming that the flow properties including the molecular mixing state vary insignificantly normal to the flow direction, the normalized LIF intensity profiles equal the toluene mass fraction profiles.

We were able to demonstrate that incomplete molecular mixing only appears within the first 7 mm downstream of the injector trailing edge in one of our preceding studies[20] by exploiting the oxygen-induced fluorescence signal red-shift.[33,43] is why LIF profiles in the very vicinity of the injector trailing edge ($d < 10$ mm) are not considered in this paper. In addition, temperature and pressure variations normal to the flow direction are evaluated from numerical results: The largest gradients in vertical direction occur in the vicinity of the nozzle throat (cf. Fig. 10c) where expansion fans interact with the wake flow. Here, the maximum deviations amount to 5 % in temperature and 10 % in pressure of the corresponding mean value. Up- and downstream the deviations are less than 2 % (temperature) and 5 % (pressure) everywhere and considered negligible regarding the fluorescence intensity.

A one-to-one comparison of normalized LIF intensity and normalized toluene mass fraction profiles from numerical simulations is given in Fig. 12. The three pro-

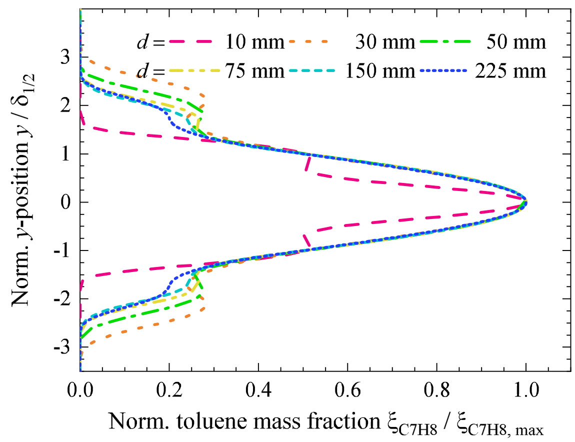

FIG. 13. Normalized toluene (C_7H_8) mass fraction profiles from numerical simulation

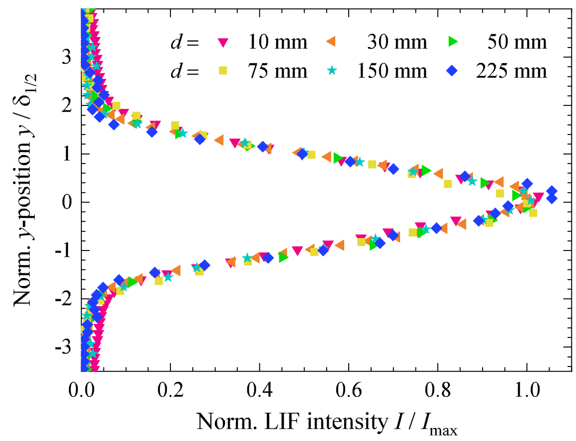

FIG. 14. Normalized toluene-LIF intensity profiles

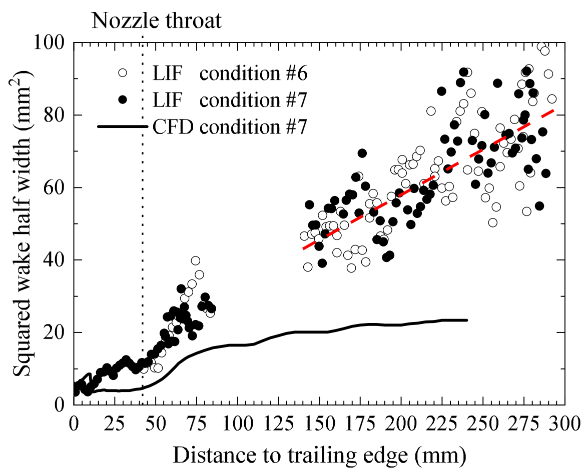

FIG. 15. Squared half-width of the wake flow. The red dashed line represents the 1/2-power law with $\Delta = 0.5\,\text{mm}^{1/2}$.

files were extracted at 10 mm, 50 mm, and 225 mm downstream of the injector trailing edge. The experimental results originate from two different measurement campaigns (open and filled symbols) with different inflow conditions #6 and #7. (The amount of tracer added to the injectant was increased to gain better signal-to-noise ratios.) Note that at $d = 10\,\text{mm}$ experimental results are only available for condition #7 because no data was recorded upstream of the nozzle throat during the other measurement campaign. Whereas the LIF profiles are, independent of the injectant amount, very smooth and almost Gaussian shaped, the simulated profiles exhibit two "side peaks" enclosing the maximum at the wake centerline that decay further downstream. As a consequence, no full self-similar state of the wake is reached within the numerical domain. This becomes more evident in Fig. 13 that illustrates normalized tracer mass fraction profiles from numerical simulation at six positions throughout the flow channel. In contrast, all normalized LIF intensity profiles approximately coincide as visualized in Fig. 14 from the first postion ($d = 10\,\text{mm}$) on revealing a self-similar behavior. This is in accordance to previous findings in our labs obtained with different setups.[13,14]

Another important wake flow characteristic is its axial growth rate. Various previous studies suggest that the half-width $\delta_{1/2}$ of a wake is proportional to the distance d to the wake generator $\delta_{1/2} \propto d^{1/2}$, the so-called 1/2-power law, irrespective of whether the co-flow is subsonic[3,12], transonic[13], or supersonic[10]. The growth rate can be determined from the slope of the squared wake half-width $\Delta = \sqrt{(\delta_{1/2}(d_1) - \delta_{1/2}(d_2))^2 / |d_1 - d_2|}$. Figure 15 depicts the half-widths determined from LIF intensity profiles throughout the test section together with numerical results. Even though the LIF intensity profiles were averaged over 200 single shots each, the experimental results scatter in the supersonic flow region. We believe that this is due to a combination of the following three reasons: First, weak oblique shocks that originate from the flange connection between module 2 and 3 locally narrow the mixing layer. Secondly, the flat-field images are prone to residual misalignment because the flow channel continuously shifts during the test day due to further thermal expansion of the test facility. Thirdly, ensemble averaging causes certain artifacts as high-frequency events ($\approx 7.5\,\text{kHz}$) are heavily undersampled (8 Hz). Therefore, for future experiments, a connecting module that decouples the channel position from the thermal expansion of the test facility is desired, as well as a trigger unit that allows for phase accurate recording. Nevertheless, the squared half width grows approximately linearly with the distance to the trailing edge (red line) and, thus, follows the 1/2-power law with $\Delta = 0.5\,\text{mm}^{1/2}$ (coefficient of determination $R^2 = 0.55$). This applies to both conditions #6 and #7 as we could not see any major differences. The effect of the base bleed on the growth rate has been also studied by Chun[14] who increased the injection mass flow ratio beyond ours (table II, last two entries). However, he also did not observe any dependence. Most likely, the injection flow rate has to be further increased to considerably affect the vortex formation and, thereby, the growth rate.

In contrast, the predicted growth rate from numerical simulation $\Delta = 0.35\,\mathrm{mm}^{1/2}$ is significantly reduced compared to the experiments. This indicates again – together with deviations in the shape of the wake profiles, in the flow properties at the wake centerline, and in the vortex shedding frequency (see above) – that the onset of vortex shedding is not well predicted.

TABLE II. Wake growth rates under various flow conditions

	Re_∞ $\times 10^5$	Ma_∞	$\dot{m}_{INJ}/\dot{m}_\infty$ g/g	Ma_{NE}	Δ $mm^{1/2}$
LIF #6	0.62	0.34	0.11 %	1.7	0.50
LIF #7	0.62	0.34	0.14 %	1.7	0.50
CFD #7	0.62	0.34	0.14 %	1.7	0.35
Wohler[13]	1.07	0.72	0.17 %	1.3	0.28
Chun[14]	1.2	0.70	0.23 %	2.1	0.17
Chun[14]	1.2	0.70	0.37 %	2.1	0.17

IV. DISCUSSION

A. Experimental results

To validate our experimental findings and to evaluate the effect of Reynolds and Mach number variations, our results are compared to results from preceeding experiments in our labs: The very same and a similarily shaped central injector have also been the object of toluene-LIF measurements in the works of Wohler[13] and Chun[14], respectively. Whereas the basic design of the flow channels by Wohler and Chun was similar to ours, the co-flow Reynolds number Re_∞ and Mach number Ma_∞ at the point of injection, the injection mass flow ratio $\dot{m}_{INJ}/\dot{m}_\infty$, and the Mach numbers at the nozzle exit Ma_{NE} were different as summarized in table II, together with the resulting wake growth rates. The highest growth rate was achieved in our measurements, the lowest with the configuration of Chun, whereas Wohler's result lays in between. This suggests that the growth rate depends above all on the free-stream Reynolds number at the point of injection since Re_∞ is increased from 0.62×10^5 (this work) to 1.07×10^5 (Wohler's work) and to 1.2×10^5 (Chun's work). The free-stream Mach number at the point of injection (compressibility effects) as well as the maximum Mach number at the nozzle exit, however, seem to have less significance. This also applies to the injected gas flow rate, at least within the range covered by these experiments. As discussed in this paper (Fig. 6), the injected mass flow rate needs to be considerably increased (beyond our experimental possibilities) to noticeably affect the vortex formation mechanism.

We showed in one of our recent numerical studies[21] that an increase in Reynolds number results in an increase in vortex shedding frequency f, while the Strouhal number stays approximately constant and the amplitudes of the induced fluctuations decrease. In addition, Chun[14] showed that the vortices significantly decrease in size with increasing Reynolds number. (Unfortunately, he was not able to analyze the growth rate of his lower Reynolds number case because the vortices interacted with the wall boundaries.) From this, we conclude that the size of the vortices and the strength of the induced fluctuations, which depend on the co-flow Reynolds number, primarily determine the growth rate of a subsonic, compressible mixing layer with low-momentum injection.

B. Numerical results

This paper shows that temperature and Mach number are globally quantitatively well predicted by the 3D URANS numerical simulation, whereas the unsteadiness of the mixing layer involving the formation of a vortex street is only qualitatively met. This qualifies the numerical results to be used for future quantitative analysis of tracer LIF measurements, which require knowledge about the pressure and temperature field. However, the simulation needs to be improved to gain a fundamental understanding of the underlying flow physics.

The results indicate that the simulation fails to correctly predict the vortex formation mechanism. This is a known issue with eddy viscosity closures[44], such as the SST turbulence model. It is generally believed that the underlying reason for this is the assumption of (locally) isotropic turbulence. Schmitt[45] even goes further and shows that the Boussinesq's turbulent viscosity hypothesis (Eq. 1) itself is violated within the wake of a square cylinder.

$$\tau_{ij} = 2\nu_t S^*_{ij} - \frac{2}{3}k\delta_{ij}, \qquad (1)$$

The Boussinesq's hypothesis is applied to the unsteady Reynolds-averaged Navier-Stokes (URANS) equations to approximate the Reynolds stress tensor τ_{ij}. It assumes that τ_{ij} and the (compressible) shear rate tensor S^*_{ij} have the same alignment. It depends further on the turbulent kinetic energy k (multiplied by the Kronecker delta δ_{ij}) and the eddy viscosity ν_t. The latter is calculated according to the applied eddy viscosity closure, in our case the SST turbulence model. Schmitt demonstrates by means of a large-eddy simulation (LES) of a square cylinder that the alignments of the two tensors τ_{ij} and S^*_{ij} deviate by $> 45°$ in the region of vortex formation and within the adjacent shear layers. Thus, the Boussinesq's hypothesis is not valid in these regions and URANS numerical simulation is not capable to accurately study the flow physics of an unsteady wake.

Therefore, a detached-eddy simulation (DES) of this setup is currently in progress. Unfortunately, the results are not expected before next year because its mesh resolution and time step requirements make the DES computationally very expensive. However, we have demonstrated in this paper that 3D URANS is capable of simulating the unsteadiness of the flow and fairly meets the measured wall static pressure, Mach number, and temperature. This makes it a valuable and affordable tool for future case studies, whereas DES is only reasonable for single point investigations.

V. CONCLUSIONS

The mixing layer of a wing-shaped central injector in a compressible accelerated nozzle flow has been investigated experimentally and numerically. Different optical measurement techniques were applied to visualize the flow structures and to measure the vortex shedding frequency, the Mach number and temperature, and the injectant distribution. As a result, a profound data set was collected that can be used for the validation of numerical results. A comparison between these data and 3D URANS simulation using the SST turbulence model revealed that our simulations fail to correctly predict the onset of vortex shedding: Both the shedding frequency and the mixing layer growth rate differ by about $-14\,\%$. In addition, no full self-similar state of the mixing layer is reached within the numerical domain, whereas the intensity profiles recorded with laser-induced fluorescence (LIF) indicate that the mixing layer starts growing self-similarly from only $d \approx 10\,\mathrm{mm}$ downstream of the trailing edge. These differences may be attributed to a violation of the Boussinesq's hypothesis in the region of vortex formation.[45] Nevertheless, the numerical results show overall good agreement ($\pm 5\,\%$ for $d > 10\,\mathrm{mm}$) regarding the Mach number and temperature distribution within the nozzle measured with laser-induced thermal acoustics (LITA). Therefore, the numerical data may be used for future quantitative analysis of complementary LIF measurements, which require knowledge of the pressure and temperature field.

Further, the mixing layer growth rate was compared to literature data[13,14] that were obtained previously in our lab with similar setups but at different (transonic) flow conditions. From this we conclude that the growth rate primarily depends on the free-stream Reynolds number at the point of injection, whereas compressibility effects and the base bleed are negligible within the considered ranges (table II).

ACKNOWLEDGMENTS

The authors kindly acknowledge the financial support of this work by the German Research Foundation (Deutsche Forschungsgemeinschaft) through the research project “Experimental and Numerical Mixing Investigations in a Compressible Nozzle Flow” (WE 2549/31 and SCHU 1369/21). Computer resources for this project have been provided by the Steinbuch Centre of Computing (SCC) at the Karlsruhe Institute of Technology (KIT).

[1] A. Roshko, “On the drag and shedding frequency of two-dimensional bluff bodies,” Tech. Rep. NACA-TN-3169 (National Advisory Committee for Aeronautics; Washington, DC, United States, 1954).
[2] A. Roshko, “Experiments on the flow past a circular cylinder at very high reynolds number,” Journal of Fluid Mechanics **10**, 345–356 (1961).
[3] I. Wygnanski, F. Champagne, and B. Marasli, “On the large-scale structures in two-dimensional, small-deficit, turbulent wakes,” Journal of Fluid Mechanics **168**, 31–71 (1986).
[4] P. W. Bearman, “Investigation of the flow behind a two-dimensional model with a blunt trailing edge and fitted with splitter plates,” Journal of Fluid Mechanics **21**, 241–255 (1965).
[5] C. J. Apelt and G. S. West, “The effects of wake splitter plates on bluff-body flow in the range $10^4 < \mathrm{R} < 5 \times 10^4$. Part 2,” Journal of Fluid Mechanics **71**, 145–160 (1975).
[6] P. W. Bearman, “The effect of base bleed on the flow behind a two-dimensional model with a blunt trailing edge,” Aeronautical Quarterly **18**, 207–224 (1967).
[7] C. J. Wood, “The effect of base bleed on a periodic wake,” The Journal of the Royal Aeronautical Society **68**, 477–482 (1964).
[8] D. Papamoschou and A. Roshko, “The compressible turbulent shear layer: an experimental study,” Journal of Fluid Mechanics **197**, 453?477 (1988).
[9] S. Barre, C. Quine, and J. P. Dussauge, “Compressibility effects on the structure of supersonic mixing layers: experimental results,” Journal of Fluid Mechanics **259**, 47?78 (1994).
[10] M. Nakagawa and W. J. A. Dahm, “Scaling properties and wave interactions in confined supersonic turbulent bluff-body wakes,” AIAA Journal **44**, 1299–1309 (2006).
[11] S. Goldstein, *Modern developments in fluid dynamics, Vol. 2* (Clarendon Press, 1950).
[12] F. M. White, *Viscous Fluid Flow, Third Edition* (Tata Mcgraw Hill, 2011).
[13] A. Wohler, B. Weigand, K. Mohri, and C. Schulz, “Mixing processes in a compressible accelerated nozzle flow with blunt-body wakes,” AIAA Journal **52**, 559–568 (2014).
[14] J.Chun, *Experimental Investigations of Injection, Mixing, and Reaction Processes in Supersonic Flow Applications*, Ph.D. thesis, Institute of Aerospace Thermodynamics, University of Stuttgart (2009).
[15] T. Winnemöller, M. Meinke, and W. Schrder, “Comparison of the mixing efficiency of different injector configurations,” Computers & Fluids **117**, 262 – 272 (2015).
[16] A. Grzona, A. Weiss, H. Olivier, T. Gawehn, A. Gülhan, N. Al-Hasan, G. Schnerr, A. Abdali, M. Luong, H. Wiggers, C. Schulz, J. Chun, B. Weigand, T. Winnemöller, W. Schröder, T. Rakel, K. Schaber, V. Goertz, H. Nirschl, A. Maisels, W. Leibold, and M. Dannehl, “Gas-phase synthesis of non-agglomerated nanoparticles by fast gasdynamic heating and cooling,” in *Shock Waves* (Springer Berlin Heidelberg, Berlin, Heidelberg, 2009) pp. 857–862.
[17] J. Richter, M. Beuting, T. Dreier, C. Schulz, and B. Weigand, “Macroscopic mixing investigation in a compressible accelerated nozzle flow using toluene tracer LIF,” in *18^{th} International Symposium on Applications of Laser and Imaging Techniques to Fluid Dynamics, Lisbon, Portugal* (2016).
[18] J. Richter, M. Beuting, C. Steinhausen, T. Dreier, C. Schulz, and B. Weigand, “Non-intrusive frequency measurements of bluff-body vortex shedding at high reynolds numbers,” in *23^{rd} International Society of Air-breathing Engines Conference, Manchester, Great Britain* (2017).
[19] J. Richter, J. Mayer, and B. Weigand, “Accuracy of non-resonant laser-induced thermal acoustics (lita) in a convergent–divergent nozzle flow,” Applied Physics B **124**, 19 (2018).

[20]M. Beuting, J. Richter, B. Weigand, T. Dreier, and C. Schulz, "Application of toluene LIF to transonic nozzle flows to identify zones of incomplete molecular mixing," Opt. Express **26**, 10266–10273 (2018).
[21]J. Richter, M. Beuting, C. Schulz, and B. Weigand, "Numerical investigation of transonic mixing behavior in the wake of a central injector at different reynolds numbers," in *48^{th} AIAA Fluid Dynamics Conference, Atlanta, GA, USA* (2018).
[22]M. Beuting, J. Richter, B. Weigand, and C. Schulz, "Experimental investigation of the influence of the pressure gradient on the transonic mixing behavior in blunt-body wakes using tracer LIF," in *48^{th} AIAA Fluid Dynamics Conference, Atlanta, GA, USA* (2018).
[23]G. Settles, *Schlieren and Shadowgraph Techniques* (Springer-Verlag Berlin Heidelberg, 2001).
[24]J. Menser, T. Dreier, S. Kaiser, and C. Schulz, "Multi-pulse rgb illumination and detection for particle tracking velocimetry [poster]," *7^{th} European Combustion Meeting, Budapest, Hungary*, (2015).
[25]A. Stampanoni-Panariello, D. N. Kozlov, P. P. Radi, and B. Hemmerling, "Gas phase diagnostics by laser-induced gratings ii. experiments," Appl. Phys. B **81**, 113–129 (2005).
[26]F. J. Förster, S. Baab, G. Lamanna, and B. Weigand, "Temperature and velocity determination of shock-heated flows with non-resonant heterodyne laser-induced thermal acoustics," Appl. Phys. B **121**, 235–248 (2015).
[27]E. Cummings, *Laser-induced thermal acoustics*, Ph.D. thesis, California Institute of Technology (1995).
[28]A. Stampanoni-Panariello, D. N. Kozlov, P. P. Radi, and B. Hemmerling, "Gas phase diagnostics by laser-induced gratings i. theory," Appl. Phys. B **81**, 101–111 (2005).
[29]E. B. Cummings, I. A. Leyva, and H. G. Hornung, "Laser-induced thermal acoustics (lita) signals from finite beams," Appl. Opt. **34**, 3290–3302 (1995).
[30]A. Hell, F. J. Förster, and B. Weigand, "Validation of laser-induced thermal acoustics for chemically reacting h2/air free jets," Journal of Raman Spectroscopy **47**, 1157–1166 (2016).
[31]S. Baab, F. J. Frster, G. Lamanna, and B. Weigand, "Speed of sound measurements and mixing characterization of under-expanded fuel jets with supercritical reservoir condition using laser-induced thermal acoustics," Experiments in Fluids **57**, 1–13 (2016).
[32]N. C. Dröske, F. J. Förster, B. Weigand, and J. von Wolfersdorf, "Thermal investigation of an internally cooled strut injector for scramjet application at moderate and hot gas conditions," Acta Astronautica **132**, 177 – 191 (2017).
[33]W. Koban, J. D. Koch, R. K. Hanson, and C. Schulz, "Oxygen quenching of toluene fluorescence at elevated temperatures," Applied Physics B **80**, 777–784 (2005).
[34]CentaurSoft, "CENTAUR^{TM}, release 12," (www.centaursoft.com).
[35]ANSYS, Inc., "ANSYS® CFX, release 18," (www.ansys.com).
[36]F. R. Menter, "Two-equation eddy-viscosity turbulence models for engineering applications," AIAA Journal **32**, 1598–1605 (1994).
[37]B. J. McBride, S. Gordon, and M. A. Reno, "Coefficients for calculating thermodynamic and transport properties of individual species," Tech. Rep. NASA-TM-4513 (National Aeronautics and Space Administration, 1993).
[38]E. W. Lemmon, I. Bell, M. L. Huber, and M. O. McLinden, "NIST Standard Reference Database 23: Reference Fluid Thermodynamic and Transport Properties-REFPROP, Version 10.0, National Institute of Standards and Technology," (2018).
[39]W. Koban, J. D. Koch, R. K. Hanson, and C. Schulz, "Absorption and fluorescence of toluene vapor at elevated temperatures," Phys. Chem. Chem. Phys. **6**, 2940–2945 (2004).
[40]S. Faust, T. Dreier, and C. Schulz, "Temperature and bath gas composition dependence of effective fluorescence lifetimes of toluene excited at 266nm," Chemical Physics **383**, 6 – 11 (2011).
[41]S. Faust, M. Goschütz, S. A. Kaiser, T. Dreier, and C. Schulz, "A comparison of selected organic tracers for quantitative scalar imaging in the gas phase via laser-induced fluorescence," Applied Physics B **117**, 183–194 (2014).
[42]T. Benzler, S. Faust, T. Dreier, and C. Schulz, "Low-pressure effective fluorescence lifetimes and photo-physical rate constants of one- and two-ring aromatics," Applied Physics B **121** (2015), 10.1007/s00340-015-6271-1.
[43]K. Mohri, M. Luong, G. Vanhove, T. Dreier, and C. Schulz, "Imaging of the oxygen distribution in an isothermal turbulent free jet using two-color toluene LIF imaging," Applied Physics B **103**, 707–715 (2011).
[44]B. A. Younis and V. P. Przulj, "Computation of turbulent vortex shedding," Computational Mechanics **37**, 408 (2005).
[45]F. G. Schmitt, "About Boussinesq's turbulent viscosity hypothesis: historical remarks and a direct evaluation of its validity," Comptes Rendus Mécanique **335**, 617 – 627 (2007).